nature portfolio

Peer Review File

A self-powered hydrogel electronic skin with decoupled multimodal sensing for closed-loop human-machine interactions

Corresponding Author: Dr Wei Zhai

This file contains all reviewer reports in order by version, followed by all author rebuttals in order by version.

Version 0:

Reviewer comments:

Reviewer #1

(Remarks to the Author)
This study stands out due it its innovative ideas, including achieving high stretchability and low modulus through sequential solvent substitution of the PVA hydrogel, amplifying vertical stress concentration and enhancing piezoionic output by over 100 times through prismatic architecture engineering, and ensuring durable hydrophilicity and improving sweat transport efficiency via hydrochloric acid treatment of the PDMS substrate. The demonstrated self-powered multimodal sensing capability, including thermogalvanic, piezoionic, and diffusion effects, is a significant advancement over existing technologies. Howeverm the completeness of the manuscript would be improved by addressing the following question:
1. This study mentions using machine learning (LSTM/CNN) for decoupling the sensing capabilities of temperature, pressure, and electrolyte. Does the signal processing and transmission circuitry require external power? If so, this potentially contradicts the paper's central claim of self-powered multimodal sensing without external power.
2. The submission of a temporal machine learning model with local attention to decouple multimodal signals is promising. However, despite the successful decoupling methodology, there appears to be a lack of fundamental exploration and quantitative explanation regarding the mutual influence (crosstalk) among the individual sensing modalities (temperature, pressure, and sweat electrolyte)

Reviewer #2

(Remarks to the Author)
The manuscript reports a poly(vinyl alcohol)-based hydrogel capable of sensing temperature, pressure, and electrolyte concentration through integrated thermogalvanic, piezoionic, and diffusion mechanisms. The authors demonstrate a machine learning–based signal decoupling model and a wearable wristband prototype with gesture-controlled robotics and haptic feedback. The functions realized are kind of interesting.

The material design is well introduced, and the characterization is comprehensive and supported by experimental data. Still, the authors should better position their platform relative to existing multifunctional hydrogel e-skins and emphasize how design advances current approaches in performance, functionality, or practical use.

In addition, the novelty and significance of the work could be better highlighted. While the multimodal hydrogel shows promising potential for use in flexible electronics and soft robotics, the application-oriented aspect of this study should be further addressed. The following issues should be further clarified:

1. The introduction discusses only the limitations of single-modal sensors but does not adequately position the work against existing multimodal sensing materials. The authors should also compare their material with current state-of-the-art multimodal hydrogels or e-skins to clarify the specific advantages and novelty of their approach.

2. In Fig. 2, the denotation of the samples is inconsistent. Some data are labeled as GS, while others as GS×2 (e.g., NMR, DSC). If GS×2 represents the final material at this stage, the sample labels across all characterizations should be unified accordingly. The authors also need to clarify why two glycerol substitution steps were performed.

3. In Fig. 3j, the sensitivity is fitted using two linear regions with an abrupt turning point. Despite the prism geometry, the hydrogel is a homogeneous material, and this current-pressure relationship would not be expected to exhibit such discontinuity. The authors should justify this model or consider a more appropriate fitting approach.

4. The current application studies showcase physiological sensing, gesture control, and haptic feedback as rather separate, independent functions. To support the claims of multimodal integration, the authors should consider a practical use-case demonstration that activates multiple functions simultaneously, rather than individual proofs of concept, to better highlight the relevance and application potential of the multimodal platform.

5. The manuscript contains several technical and formatting errors that require careful correction, including:
Line 347: “hydrogen e-skin”
Figure 4d: “m mol L^{-1}” should be “mmol L^{-1}.”
In Fig. 3h, labels are not fully visible.

6. Supplementary results should further include: readout circuits schematics of temperature, pressure, and electrolyte concentration(sweat) sensing. Supplementary video is kind of simple, more demonstration videos should be further enriched by adding 1)pulse monitoring, 2) grasping a paper cup illustrated in fig5.h, 3) a full demonstration of complex robot arm control/manipulation as illustrated in Fig. 5a, in addition, after hand gesture recognition, a notable delay of the robot arm execution could be observed, authors are required to further discuss the reason behind, and how to mitigate the delay, 4) other videos showcase the novelty of this work.

Reviewer #3

(Remarks to the Author)
In this manuscript, Bai et al. report a polyvinyl alcohol hydrogel synthesized by a sequential solvent exchange process to achieve a highly soft, tough, and stretchable material. They demonstrate that their PVA hydrogel is responsive to a wide variety of stimulus, including temperature, mechanical, and ionic strength, which could make it an elegant single material solution for multimodal sensing.
However, while the team presented the use of an active multimodal signal generator that employs machine learning to attempt to decouple confounding crosstalk between stimuli, rigorous characterization should also be conducted to understand how the sensor is influenced by various stimuli. Additionally, the supporting demonstrations for their human-machine interface should be extensively reported. The authors should address the following comments before further consideration.

1. The authors note that “the PVA hydrogel is engineered into a novel prismatic architecture.” This structure does not appear to be novel as in the recent report (Nat Commun 2023, 14, 2907), and other similar pyramidal structures are commonly employed in pressure sensors.

2. The sequential solvent substitution process does not appear to have “clear advantages” over other methods, such as the solvent-exchanged-assisted wet annealing in their reference (Adv. Mater., 2023, 2210624). Similarly, this work introduced subsequential solvent exchange of PVA hydrogels from DMSO, glycerol, and an aqueous solution. Additionally, by tuning the solvent-exchange wet annealing process the work reported PVA hydrogels with similar properties: 100kPa stiffness, MJ/m3 toughness, 1000% strain.

3. In figure 2j, the graph comparing properties of PVA hydrogels fabricated with other processes does not appear to be accurate, since solvent-exchanged-assisted wet annealing can similarly produce comparable soft hydrogels with <1MPa stiffness as mentioned.

4. For clarification, the authors note that “Electrolyte sensing was enabled by the diffusion effect, where temperature gradients led to differential ion diffusion.” Did they mean that ionic gradients lead to ion diffusion?

5. In figure S11, why is there still a current density when electrode distance = 0mm? Aren’t the electrodes shorted?

6. Could the authors clarify this calculation: “the maximum output power density (Pmax) was calculated as 19 μW·m-2·K-2,” since this value and units differ from the power density in figure 3d.

7. In figure 3g, how does the prismatic structure result in 100x sensitivity? Is this for the same load or the same strain?

8. How does the prismatic structure affect the performance of thermogalvanic and electrolyte sensing compared to cubed structure?

9. Critically, for simultaneous multimodal sensing, characterizations should be conducted while manipulating one stimulus at a time to observe their influence on the current output measurements. For instance, ionic concentration of NaCl can also influence the sensitivity of thermogalvanic and piezoionic effects.

In figure 3d, how is this signal decoupled into the temperature, pressure and Na concentrations? It seems that the compound

current raw recordings should simply be a superposition from all the inputs from thermogalvanic, piezoionic, and electrolyte stimuli. The compound signal does not appear to encode any of the high frequency responses in the plot of the current corresponding to pressure below. Likewise, the lower frequency current contributions from the temperature sensing component does not in the compound recording.

It seems unclear how different stimuli together are influencing the output. Rather than solely relying on a machine learning to "decouple" these, rigorous characterization should be further investigated.

10. In figure 5g, does the sensor contact the heat and cold source? Why is there no apparent change in the current recording in response to pressure?

11. Are there any supporting videos for figure 5f for real-time linear motor control from sensor feedback? Are there additional videos to accompany figure 5h to show responsive robotic hand control according to feedback? Further supporting videos should better demonstrate "closed-loop" functionality.

Version 1:

Reviewer comments:

Reviewer #1

(Remarks to the Author)
The authors fully addressed the comments raised by all the reviewers. This manuscript can be published without further revisions.

Reviewer #2

(Remarks to the Author)
Authors have well addressed my questions, get no further questions.

Reviewer #3

(Remarks to the Author)
The authors have fully addressed my previous comments.

Response Letter

Manuscript title: A self-powered hydrogel electronic skin with decoupled multimodal sensing for closed-loop human-machine interactions

Dear Editor and Reviewers:

We are sincerely grateful to the editor and reviewers for taking the time to meticulously review our manuscript and provide constructive feedback. Your comments have been instrumental in enhancing the depth and rigor of our study. In response to the reviewers' valuable suggestions, we have undertaken extensive revisions to our manuscript. These revisions include:

1. **Enhancement of Experimental Data**: We have augmented our experimental data to provide a more robust foundation for our findings, ensuring that the results are both comprehensive and reliable.

2. **Clarification of Mechanistic Explanations**: We have refined our explanations of the underlying mechanisms to ensure precision and clarity, thereby enhancing the reader's understanding of our research.

3. **Supplementation of Demonstration Videos:** We have included additional demonstration videos to visually present the closed-loop applications of our multimodal sensing and feedback system, thereby providing a more intuitive understanding of the integrated sensing-feedback process.

We have presented a comprehensive point-by-point response to all comments. We are confident that these revisions have significantly bolstered the quality of our manuscript.

We appreciate the opportunity to revise our work for consideration in *Nature Communications*. We believe that our manuscript is now better positioned to contribute to the scientific discourse in your esteemed journal.

Reviewer #1:

This study stands out due it its innovative ideas, including achieving high stretchability and low modulus through sequential solvent substitution of the PVA hydrogel, amplifying vertical stress concentration and enhancing piezoionic output by over 100 times through prismatic architecture engineering, and ensuring durable hydrophilicity and improving sweat transport efficiency via hydrochloric acid treatment of the PDMS substrate. The demonstrated self-powered multimodal sensing capability, including thermogalvanic, piezoionic, and diffusion effects, is a significant advancement over existing technologies. However, the completeness of the manuscript would be improved by addressing the following question:

Response: We sincerely appreciate the reviewer's positive assessment of our work, including the fabrication strategy, structural design, multifunctionality, and application demonstrations. We have carefully considered all the concerns raised, and our point-by-point responses are provided below.

Comment 1.1: This study mentions using machine learning (LSTM/CNN) for decoupling the sensing capabilities of temperature, pressure, and electrolyte. Does the signal processing and transmission circuitry require external power? If so, this potentially contradicts the paper's central claim of self-powered multimodal sensing without external power.

Response: Thanks for your insightful comment. We agree that the original, undefined description of "self-powered sensing" in the manuscript may cause misunderstanding. In this work, the term "self-powered" refers to the hydrogel sensing unit, which can autonomously generate electrical signals through thermogalvanic, piezoionic, and diffusion-driven mechanisms without any external power supply.

The AMSG wristband integrates several components, including a PVA-hydrogel-based electronic skin, which functions as the self-powered signal generation unit, signal processing circuitry, and a wireless transmission module. As shown in Fig. R1, the hydrogel produces stimulus-dependent current outputs under temperature, pressure, and electrolyte conditions, confirming that the hydrogel module can spontaneously produce potential differences and drive current in external circuits, thereby operating in a fully self-powered manner. This definition is consistent with the widely accepted criteria for self-powered sensors [Nat. Commun. 15, 530 (2024); Sci. Adv. 10, eadq8989 (2024)]. The potential misunderstanding comes from the processing and signal transmission modules. We acknowledge that commercial Wi-Fi chips and front-end signal processing require external power. At present, commercially available Wi-Fi transmitters typically require a minimum supply voltage of 3.3 V and a current of no less than ~300 mA, which exceeds the output capability of current self-powered

systems based on thermoelectric, triboelectric, or piezoelectric mechanisms [Adv. Mater. 37, 2416897 (2025); Adv. Funct. Mater. 33, 202303562 (2023)]. In addition, the final signal processing and decoupling, along with program control and software, must still be performed on a computer. Even so, our design substantially reduces the external power demand compared with conventional resistive and capacitive sensors that require continuous power for both sensing and communication [for example, Adv. Mater. 33, 2102069 (2021)].

Looking forward, we will work to enhance the hydrogel's self-driven power output; alternatively, to the best of our knowledge, ultra-low-power Wi-Fi communication chips are currently under development and may become available. By combining improved self-powered conversion efficiency with next-generation low-power communication modules, a fully self-powered wireless sensing system may be feasible soon.

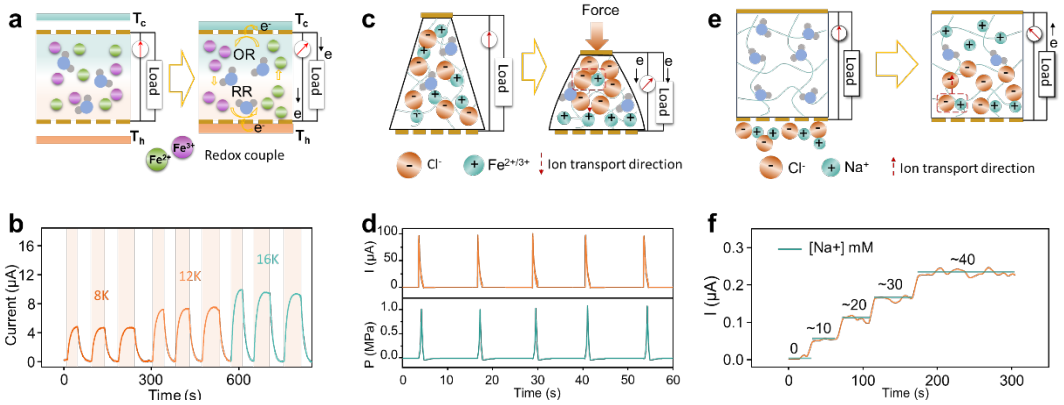

Fig. R1. Multimodal sensing capabilities. **a** Schematic illustration of the thermogalvanic effect as the temperature sensing mechanism. **b** Self-powered current variation of PVA hydrogels under different temperature differences. Darker areas indicate the presence of a temperature difference. **c** Schematic of the piezoionic effect for pressure sensing. **d** Self-powered current variation based on the piezoionic effect under pressure. **e** Schematic of the diffusion effect for sweat detection. **f** Current generated by sodium ions at different concentrations based on ion diffusion.

To clarify the definition, we have revised the description on page 3, lines 83-85 of the manuscript: *"Notably, the thermogalvanic, piezoionic, and diffusion effects support both sensing and self-powering, enabling the hydrogel sensing unit to actively generate stimuli-responsive electrical signals."*.

Comment 1.2: The submission of a temporal machine learning model with local attention to decouple multimodal signals is promising. However, despite the successful decoupling methodology, there appears to be a lack of fundamental exploration and

quantitative explanation regarding the mutual influence (crosstalk) among the individual sensing modalities (temperature, pressure, and sweat electrolyte).

Response: Thanks for your insightful comment on the multimodal sensors. We agree that a fundamental and quantitative investigation of the mutual influence among different sensing modalities (temperature, pressure, and sweat electrolyte) can further strengthen the understanding of our multimodal hydrogel system.

These sensing mechanisms originate from distinct driving forces: the thermogalvanic effect arises from temperature-gradient driven redox potential differences, the piezoionic effect is triggered by stress-induced ionic polarization, and the diffusion effect results from concentration-driven ion migration. According to liquid thermoelectric theory, the Seebeck coefficient $S_e = \Delta E/\Delta T = \Delta S_{rc}/nF$, where ΔSrc is the entropy change of the redox couple, n is the number of transferred electrons, and F is the Faraday constant [*J. Mater. Chem. A* **10**, 19690–19698 (2022)]. Within the moderate temperature range used in this work, the thermovoltage increases proportionally with the temperature difference. In contrast, the pressure-driven piezoionic effect reflects transient directional ion migration caused by local deformation of the polymer network. Smaller cations migrate more rapidly through the polymer network than larger anions, leading to charge imbalance and the formation of an internal electric field. This ion redistribution generates local concentration and potential gradients, and the ionic chemical potential gradient scales with the applied stress. Similarly, the diffusion-induced signal arises from Na^+ transport follows Fick's law and scales linearly with the external Na^+ concentration gradient, and the microchannel design ensures stable mass transport without reaching adsorption saturation in the tested range. Consequently, these three mechanisms operate independently at different temporal scales, enabling independent responses within the same material system.

Although these driving forces operate independently, minor interactions may still occur as the same ionic species can participate in different processes. To quantify this interference, we conducted additional controlled experiments as follow.

Experiment 1: Crosstalk between temperature and pressure responses

To evaluate the potential crosstalk between temperature and pressure responses, we measured the piezoionic current under different temperature differences (Fig. R2a and R2b). When the hydrogel was fixed at 30 °C without applying a temperature difference, pressures of 2, 4, 6, and 8 kPa generated ionic piezoelectric currents of 0.8, 1.7, 2.3, and 2.7 μA, respectively. A baseline thermoelectric current was generated as ΔT increased. However, the pressure-induced current variations (ΔI) remained almost unchanged, indicating that the pressure-driven ionic response is independent of the thermal stimuli.

This independence could be attributed to the distinct response mechanisms: the thermoelectric response originates from temperature-driven redox potentials, involving

electron transfer at the electrode interface and requiring several seconds of reaction time. In contrast, the piezoelectric response arises from rapid and mechanically induced local ionic polarization, thus enabling short-range ion migration within milliseconds.

Experiment 2: Crosstalk between pressure and sweat electrolyte responses

As shown in Fig. R2c and R2d, although increasing Na^+ concentration produced higher diffusion currents, the pressure-induced ΔI remained essentially constant across all tested concentrations. Similarly, this independence can be attributed to the fundamental differences between the two mechanisms. The diffusion current is a slow and steady-state process driven by concentration gradients, whereas the pressure response, as discussed before, is a rapid, stress-induced transient ionic polarization generated during the elastic compression of the hydrogel. The two processes occur on distinct timescales and follow different transport pathways, and therefore do not interfere with each other. As a result, the pressure-induced piezoionic current remains essentially unaffected by Na^+ concentration.

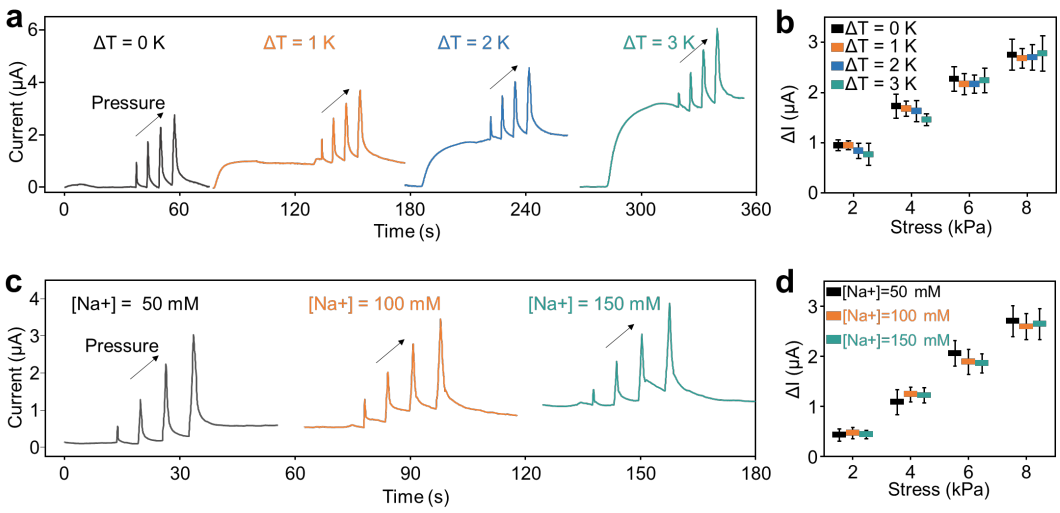

Fig. R2. a Piezoionic current at different temperature levels, where the cold end temperature is set to 30 °C, while the hot end temperatures are set to 30, 31, 32, and 33 °C, respectively. The applied pressures are 2, 4, 6, and 8 kPa, respectively. **b** Relationship between pressure and current variation (ΔI) at different temperature levels (ΔT). **c** Piezoionic current under different Na^+ concentrations, with applied pressures of 2, 4, 6, and 8 kPa, respectively. **d** Relationship between pressure and current variation (ΔI) under different Na^+ concentrations.

Experiment 3: Crosstalk between temperature and sweat electrolyte responses

We further examined the possible crosstalk between temperature and sweat electrolyte responses. As shown in Fig. R3, increasing Na^+ concentration enhances the thermogalvanic current, and larger temperature differences also increase the diffusion-driven current. This coupling originates from the synergy of the Soret effect and the thermogalvanic effect [Science 368, 1091 – 1098 (2020)]. The total ionic flux can be

described by $J = -D\nabla c - D_T c\nabla T$, where D_T is the thermal diffusion coefficient. When a temperature difference is applied, Na^+ ions preferentially migrate toward the colder end, generating an additional directed ion flux. At the same time, elevated temperature enhances the diffusion of Na^+ ions driven by concentration gradients. As a result, within a certain temperature range, the thermogalvanic effect and concentration diffusion act together.

In our system, at Na^+ concentrations of 50, 100, and 150 mM, the thermoelectric currents induced by a 1 K temperature difference were 0.89, 1.05, and 1.39 μA, respectively. Under a 2 K temperature difference, the corresponding currents increased to 1.82, 2.10, and 2.70 μA. Compared with the baseline thermoelectric current of 0.80 μA in the absence of Na^+, these results suggest that each 50 mM increase in Na^+ concentration contributes an additional ~0.15 $\mu A \cdot K^{-1}$ to the thermoelectric response.

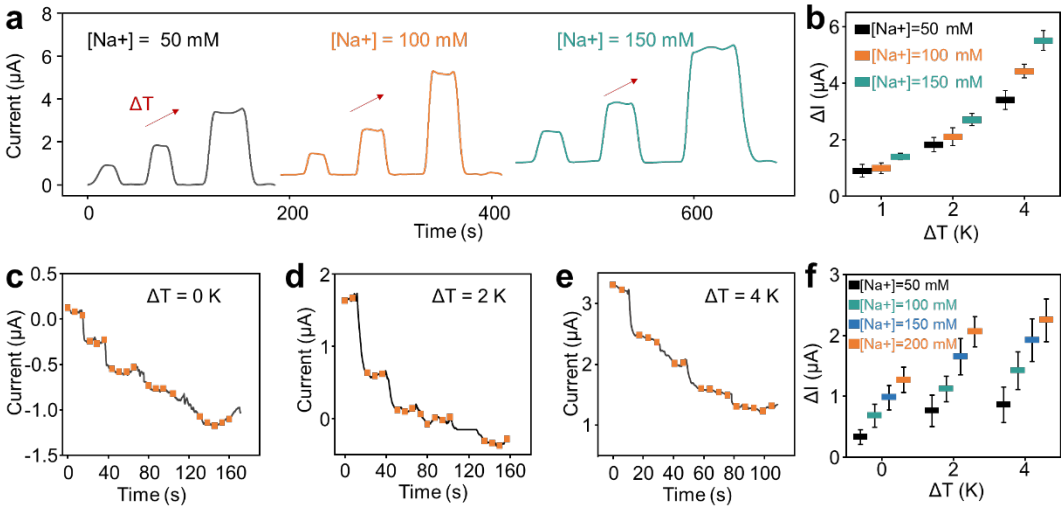

Fig. R3. a Thermoelectric current induced by different temperature differences at various Na^+ concentrations, with the hot junction temperature fixed at 30 °C. The cold junction temperatures were set to 29, 28, and 26 °C, respectively. **b** Thermoelectric response under different Na^+ concentrations. Time-dependent diffusion current curves during stepwise absorption of 50μL Na^+ solutions at different temperature differentials: (**c**) 0 K, (**d**) 2 K, (**e**) 4 K. The cold junction temperature was fixed at 30 °C. The hot junction temperature was set to 30, 32, and 34 °C, respectively. **f** Effect of Na^+ concentration on diffusion current variation (ΔI) under different temperature differences (ΔT).

In summary, the thermoelectric and piezoionic responses, as well as the diffusion and piezoionic responses, operate independently due to their distinct driving forces and characteristic timescales. Although diffusion and thermoelectric signals exhibit a predictable linear coupling under temperature gradients, this behavior does not affect the separability of the three physical signals. The linearity ensures that the machine-learning model can reliably decouple and reconstruct each sensing modality.

This discussion has been added to page 19 of the manuscript, lines 442–456, as follows: *"To investigate potential crosstalk between the signals, we applied repeated pressure stimuli of 2, 4, 6, and 8 kPa under different temperature gradients (Fig. R2a) and different Na+ concentrations (Fig. R2b). The piezoionic current increments remained nearly identical in all cases, indicating that the pressure-induced ionic signals were not affected by variations in temperature nor Na^+ concentration. This independence arose from the distinct physical origins of the signals: the piezoionic current was generated by transient, mechanically induced ionic polarization, whereas the thermoelectric and diffusion currents were driven by inherently slow, steady-state processes. A minor interaction was observed between the temperature and Na^+ concentration signals: a larger temperature gradient produced higher diffusion currents because temperature not only drove the thermogalvanic potential but also triggered the Soret effect, causing additional Na+ migration along the thermal gradient (Fig. R3). Nevertheless, within the temperature range investigated in this work, both temperature- and concentration-driven diffusion remained in the linear regime, which allowed their contributions to superimpose proportionally and produce a stable, predictable current response."*

Supplementary Fig. S35 and Fig. S36 include the experimental results corresponding to Fig. R2 and Fig. R3.

Reviewer #2:

The manuscript reports a poly (vinyl alcohol)-based hydrogel capable of sensing temperature, pressure, and electrolyte concentration through integrated thermogalvanic, piezoionic, and diffusion mechanisms. The authors demonstrate a machine learning–based signal decoupling model and a wearable wristband prototype with gesture-controlled robotics and haptic feedback. The functions realized are kind of interesting.

The material design is well introduced, and the characterization is comprehensive and supported by experimental data.

Still, the authors should better position their platform relative to existing multifunctional hydrogel e-skins and emphasize how design advances current approaches in performance, functionality, or practical use.

In addition, the novelty and significance of the work could be better highlighted. While the multimodal hydrogel shows promising potential for use in flexible electronics and soft robotics, the application-oriented aspect of this study should be further addressed. The following issues should be further clarified:

Response: We sincerely appreciate the reviewer's positive evaluation of our work. Your constructive and insightful suggestions have helped us further refine and improve the manuscript. We have carefully addressed all comments and have revised the manuscript accordingly. The detailed responses and revisions are provided below.

Comment 2.1: The introduction discusses only the limitations of single-modal sensors but does not adequately position the work against existing multimodal sensing materials. The authors should also compare their material with current state-of-the-art multimodal hydrogels or e-skins to clarify the specific advantages and novelty of their approach.

Response: Thank you for highlighting the important point. To better position our work in relation to existing multimodal sensing platforms, we have revised the introduction to explicitly compare our material with state-of-the-art multimodal hydrogels and e-skins.

A comparative discussion has been added on Page 3, Lines 59–67. The revised text is shown below: *"Recent advances in multimodal sensors and electronic skins have demonstrated simultaneous perception of temperature, pressure, strain, and humidity by incorporating ionic conductors, conductive polymers, or hybrid nanocomposites (Table R1). However, most existing single-component multimodal sensors suffer from asynchronous signal acquisition and redundant outputs, causing significant coupling errors and reduced sensing accuracy. They also remain limited in system-level*

integration, often lacking capabilities of remote operation and independent energy supply. In addition, only a few prototypes have achieved closed-loop perception and feedback, which is essential for practical human-machine interaction."

We also added Table R1 to Table S1 of the Supplementary Information to provide a clearer comparison with representative multimodal sensors.

Table R1. Comparison of Flexible Sensors

Refs	Self-powered	Multimodal sensing	Single-unit	Wearability	Response time
This work	√	√	√	Strain: 830% Modulus: 300 kPa	37 ms
[1] *Adv. Mater*. 34, 2205249 (2022)	×	√	√	Rigid	100 ms
[2] *Adv. Funct. Mater*. 34, 2314419 (2024)	√	×	√	Strain:530%	230 ms
[3] *Nat. Commun.* 16, 5689 (2025)	×	√	×	Rigid	N/A
[4] *Nat. Commun.* 16, 591 (2025).	×	×	×	Strain: 50% Modulus: 17 MPa	12 ms

Comment 2.2: In Fig. 2, the denotation of the samples is inconsistent. Some data are labeled as GS, while others as GS×2 (e.g., NMR, DSC). If GS×2 represents the final material at this stage, the sample labels across all characterizations should be unified accordingly. The authors also need to clarify why two glycerol substitution steps were performed.

Response: Thank you for your careful review. In the revised manuscript, we have corrected the sample labeling. "GS" now consistently refers to PVA organogel obtained after two successive glycerol substitution processes.

We also clarified the rationale for performing two substitution cycles. During the glycerol substitution process, we compared the Fourier transform infrared (FTIR) spectra of the DMSO–GS PVA organogel obtained after substitution once with those of the GS PVA organogel obtained after substitution twice (Fig. R4a). The twice-substituted GS organogel exhibited a more pronounced redshift and broader O–H stretching vibration band, indicating stronger and more uniform hydrogen-bonding interactions. Macroscopically, the DMSO–GS organogel appeared slightly warped due to uneven shrinkage caused by incomplete glycerol displacement (Fig. R4b), whereas the twice-substituted organogel showed a regular block-like shape. These observations

indicate that two substitution cycles are required for thorough solvent exchange and for producing a structurally uniform GS organogel.

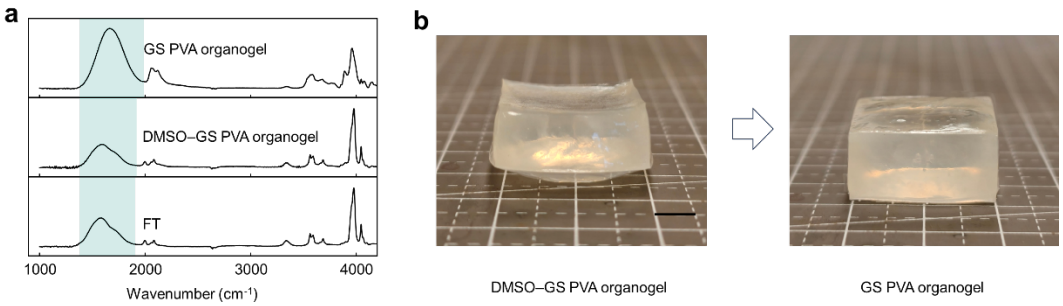

Fig. R4. a Fourier transform infrared spectra of the FT PVA Organogels, DMSO-GS PVA Organogels and GS Organogels. **b** Comparison photos of PVA Organogels after single and double glycerol displacement.

Fig. R4 has been added to the Supplementary Information as Fig. S4. The method description has been updated as follows: "*Hydrogel Fabrication—GS PVA Organogels: PVA powder was dissolved in DMSO under vigorous stirring at 95°C to form a 15 wt.% solution. After degassing via sonication for 2.5 h, the obtained clear solution was cast into 3D-printed molds and frozen at -80°C for 2 h. The frozen gels were then immersed in glycerol at room temperature for 24 h to initiate substitution between DMSO and glycerol, with the glycerol replaced at least twice to ensure thorough exchange. The resulting hydrogel was designated as GS.*"

Additionally, Fig. 2 in the manuscript has been updated as Fig. R5.

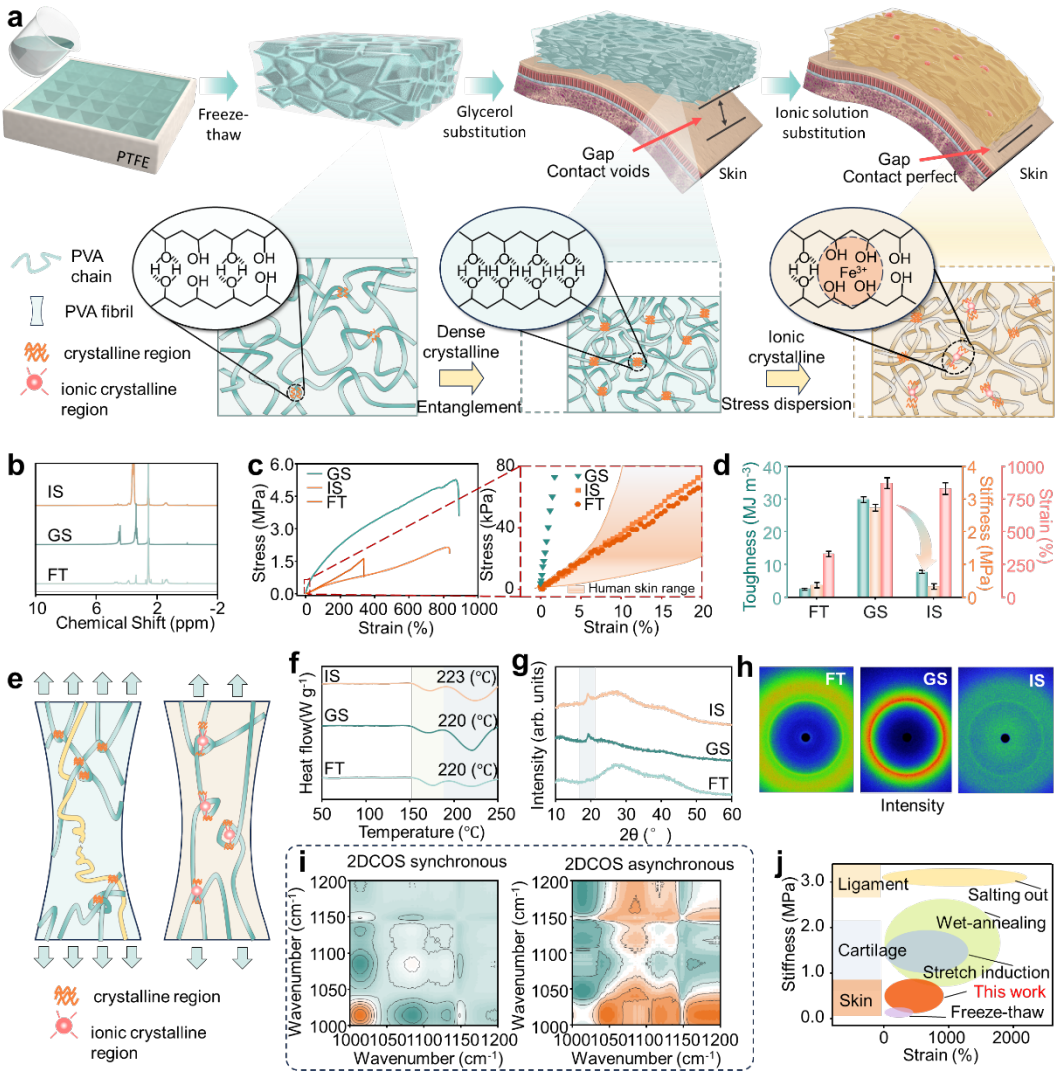

Fig. R5. Preparation and material properties of PVA hydrogels through sequential solvent substitution. a Schematic illustration of the fabrication process, including freeze-thawing (FT), glycerol substitution (GS), and ionic substitution (IS), leading to progressively enhanced hydrogel networks. **b** ^{1}H-NMR spectra of FT, GS, and IS in DMSO-d_6 at 295 K. **c** Tensile stress–strain curves of PVA hydrogels after different solvent substitution treatments, compared to the range of human skin (orange shaded region). **d** Toughness and stiffness of the hydrogels across different treatments. **e** Schematic of the mechanical enhancement mechanism involving dense crystalline and ionic crystalline regions. **f** DSC thermograms of FT, GS, and IS. **g** XRD profiles of FT, GS, and IS. **h** WAXS patterns showing the crystallinity evolution among FT, GS, and IS. **i** Synchronized and asynchronized 2D-COS maps of FT, GS, and IS, where red and blue indicate positive and negative intensity, respectively. **j** Comparison of hydrogel toughness achieved in this study with that of various reported hydrogels and biological tissues.

Comment 2.3: In Fig. 3j, the sensitivity is fitted using two linear regions with an abrupt turning point. Despite the prism geometry, the hydrogel is a homogeneous material, and

this current-pressure relationship would not be expected to exhibit such discontinuity. The authors should justify this model or consider a more appropriate fitting approach.

Response: Thanks for your insightful suggestion. We agree that, given the homogeneous nature of the hydrogel, its current-pressure relationship should be continuous. Continuous fitting may be more appropriate than fitting the data in separate intervals. We adopted a more suitable fitting method referenced in literature [Adv. Mater. 36, 2406235 (2024)]. The updated fitting yields a continuous current-pressure curve, as shown in Fig. R6.

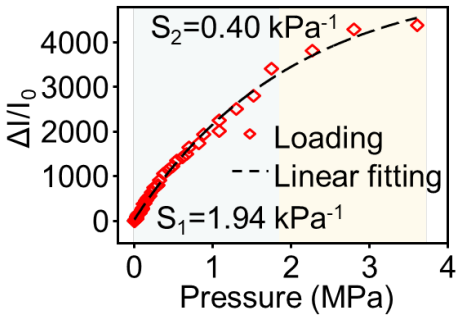

Fig. R6. Relative current change as a function of applied pressure.

Fig R6 has replaced the original Fig. 3j in the manuscript. The revised description is now on page 14, lines 340–342: *"As shown in Fig. 3j, the hydrogel exhibited a continuous current-pressure response, showing a higher sensitivity of 1.94 kPa⁻¹ at pressures below 2 MPa and 0.4 kPa⁻¹ above 2 MPa."*

Comment 2.4: The current application studies showcase physiological sensing, gesture control, and haptic feedback as rather separate, independent functions. To support the claims of multimodal integration, the authors should consider a practical use-case demonstration that activates multiple functions simultaneously, rather than individual proofs of concept, to better highlight the relevance and application potential of the multimodal platform.

Response: Thank you very much for this valuable suggestion. To better demonstrate the multimodal integration, we have designed a use-case scenario that combines physiological monitoring, gesture-based robotic control, and haptic feedback in a single workflow (Video 5). Video 5 has been uploaded as one of the supplementary materials.

In this demonstration, the robotic hand carries out experimental operations in a potentially hazardous environment, while the operator remains in a protected area and controls the process through a transparent safety enclosure. During the task, the operator can perceive both the temperature of the contacted objects and the applied gripping force in real time. We believe that this integrated demonstration more clearly

illustrates the practical relevance of our multimodal platform for future applications in safety-critical and remote-operation environments.

Comment 2.5: The manuscript contains several technical and formatting errors that require careful correction, including:

Line 347: “hydrogen e-skin”

Figure 4d: “m mol L^{-1}” should be “mmol L^{-1}.”

In Fig. 3h, labels are not fully visible.

Response: Thank you for your careful review of the images and text. We have corrected all noted technical and formatting issues, and conducted a thorough re-examination of the manuscript.

Specifically, Page 15, line 359: “hydrogen e-skin” has been revised to “hydrogel e-skin”, all instances of “m mol L^{-1}” have been standardized to “mmol L^{-1}”, including: Page 21, line 506: “10–90 mmol L^{-1}” Page 21, line 511: “90 mmol L^{-1}”. Additionally, Fig. 4 has been updated as Fig. R7, and the visibility issue in Fig. 3h has been resolved and replaced with Fig. R8.

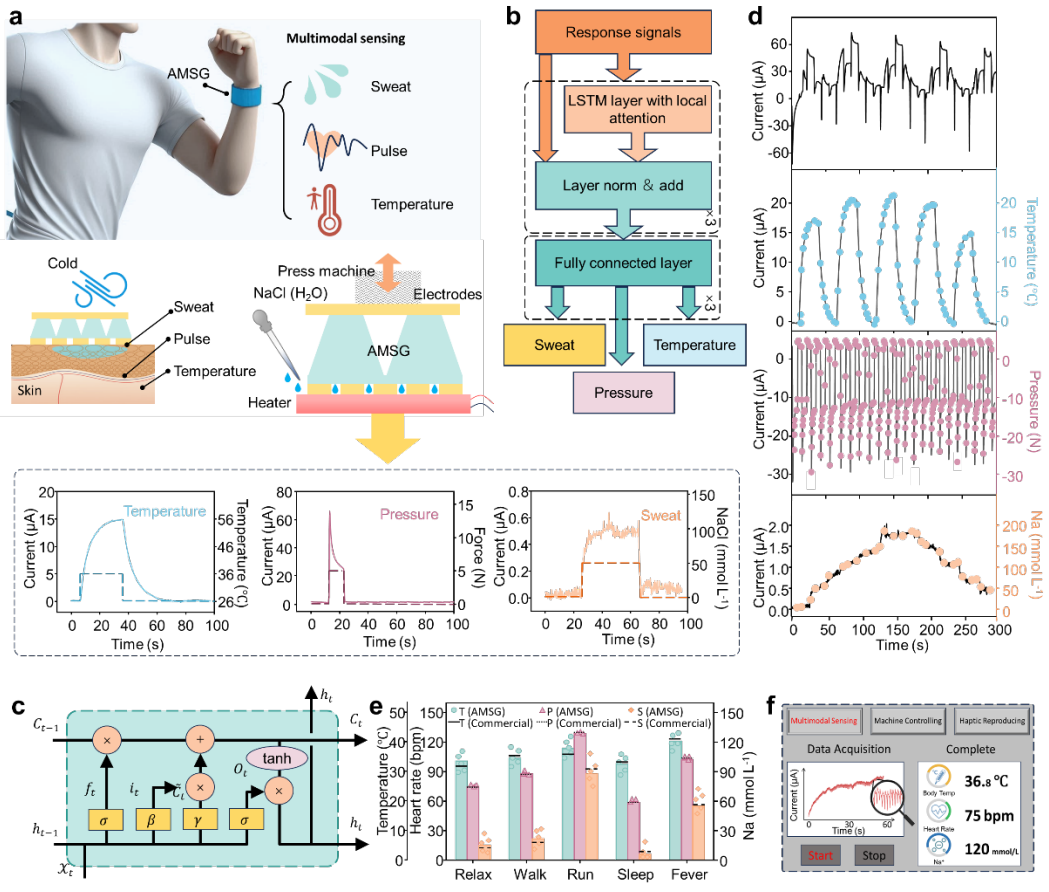

Fig. R7. Multimodal physiological sensing decoupled via a machine learning model. **a** Schematic illustration of the AMSG wristband interface for multimodal sensing of body temperature, pulse rate, and sweat secretion, simulated by individually applying temperature, pressure, and Na^+ electrolyte stimuli to obtain their characteristic signals. **b** Architecture of the machine learning-based signal decoupling model, featuring three LSTM layers with local attention and three fully connected layers for extracting and decoupling the signal features of each stimulus independently. **c** Internal structure of the LSTM network. **d** Comparison of compound signals under multiple simultaneous stimuli and their decoupled components. **e** Multimodal monitoring of body temperature, pulse rate, and sweat Na^+ concentration across various activity states (relax, walk, run, sleep, fever), benchmarked against commercial devices. **f** User interface displaying the real-time waveforms of multimodal signals and corresponding monitoring outputs.

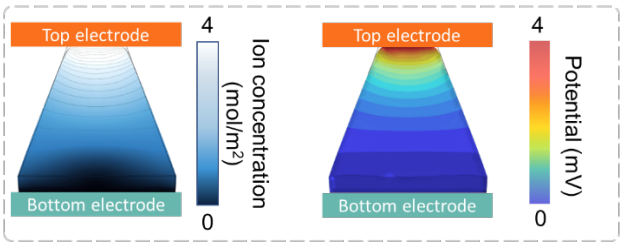

Fig. R8. COMSOL simulation of ion concentration gradients and potential distributions under pressure.

Comment 2.6: Supplementary results should further include: readout circuits schematics of temperature, pressure, and electrolyte concentration(sweat) sensing. Supplementary video is kind of simple, more demonstration videos should be further enriched by adding 1)pulse monitoring, 2) grasping a paper cup illustrated in fig5.h, 3) a full demonstration of complex robot arm control/manipulation as illustrated in Fig. 5a, in addition, after hand gesture recognition, a notable delay of the robot arm execution could be observed, authors are required to further discuss the reason behind, and how to mitigate the delay, 4) other videos showcase the novelty of this work.

Response: Thank you very much for your thoughtful comments. We have added the readout circuit schematics for temperature, pressure, and electrolyte (sweat) sensors, provided more demonstration videos, and addressed the robot arm latency issue through corresponding discussion and optimization.

As shown in Figure R9, the signal processing and transmission module consists of a sensing unit and a sampling processing unit. The sensing unit converts physical stimuli into electrical signals, which are then amplified by a preamplifier, passed through a bandpass filter to remove noise, and subsequently digitized via a 24-bit analog-to-digital converter. The digital signal is routed through a channel selection module to the

microcontroller unit (MCU). Acting as the core controller, the MCU coordinates peripheral devices via I²C bus and I/O control, and communicates with the Wi-Fi module through a UART interface for wireless data transmission. The circuitry for each module is illustrated in Figure R10.

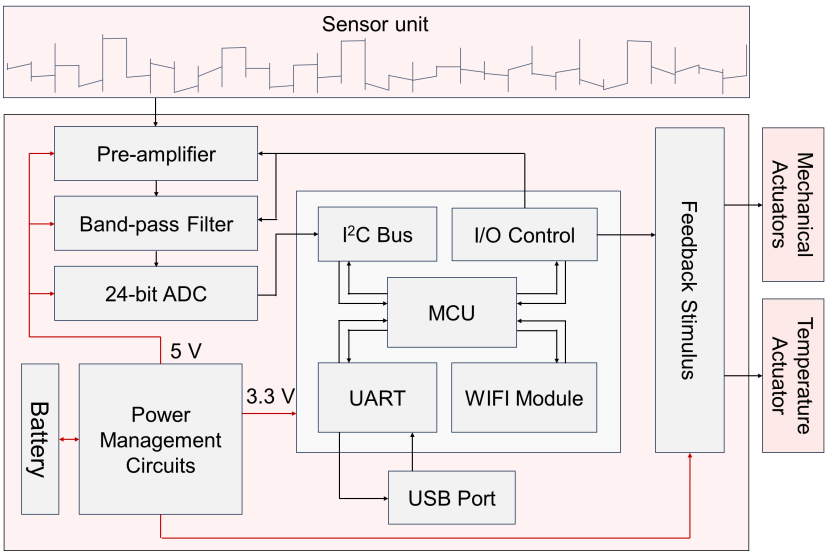

Fig. R9. Architecture of the multimodal sensing and feedback system, including signal processing, transmission, and power management.

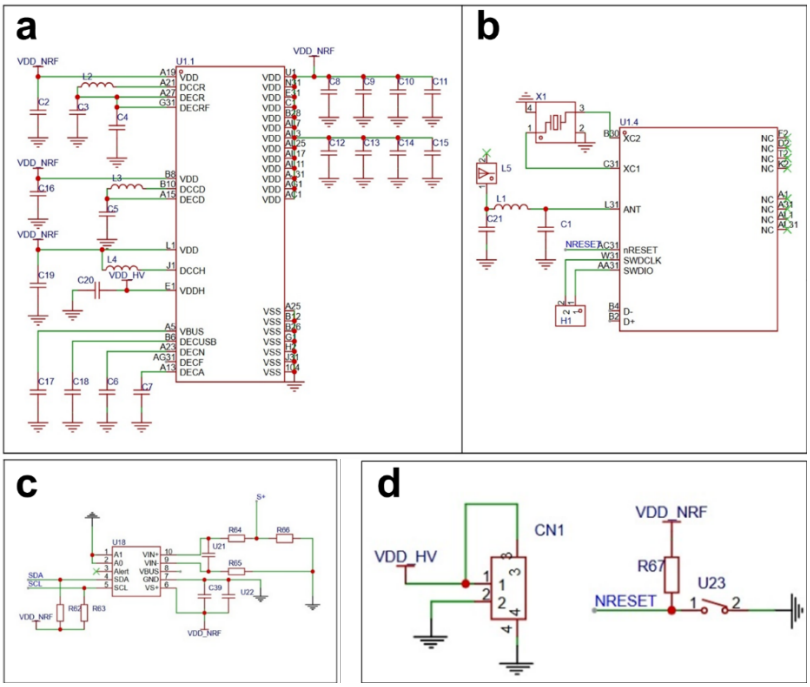

Fig. R10. Circuit Design of Wireless Current Acquisition Module. a Control and Data Processing Module. **b** Wireless Transmission Module. **c** Data Acquisition Module. **d** Power Supply and Reset Module.

We also sincerely appreciate your careful examination of our supplementary video. The latency issue between gesture recognition and robotic arm execution primarily originated from the complex model design and the low data processing efficiency of the terminal GPU. Specifically, our original workflow involved segmenting one-dimensional signals, rendering them into images using a graphics library for storage, and then reloading them for CNN recognition.

To reduce end-to-end latency, we redesigned the workflow from “image rendering and CNN classification” to “segmented one-dimensional sequence and direct machine learning recognition”. This modification preserves the recognition accuracy while significantly shortening both preprocessing and inference times. We also optimized the terminal GPU to achieve faster processing capabilities.

In addition, we have added Supplementary Videos V1–V5 to provide a more comprehensive demonstration of AMSG’s functionality. Specifically:

V1-AMSG for Multimodal Signal Sensing. Demonstrates the capability of AMSG to monitor human pulse, body temperature, and Na^+ levels in sweat.

V2-AMSG for Robotic Arm Control. Shows how the AMSG senses gesture-induced motion signals and recognizes them via machine learning to control robotic arm movements.

V3-AMSG for Temperature and Pressure Sensing. Illustrates that the AMSG mounted on the robotic arm can sense the object’s temperature and contacted pressure during approaching, contacting, and grasping.

V4-Temperature and Pressure Reproduction at the Fingertips of Robotic Arms. Demonstrates the intuitive feedback of different temperatures and grip forces during the grasping process, where the temperature change at the wristband is provided by a miniature Peltier element, and the vibration is generated by a linear vibration motor.

V5-A Closed-loop Human-machine Interaction Demonstration of AMSG for Sensing, Control, and Feedback. Presents a remote-operation scenario involving hazardous chemicals handling, integrating physiological data monitoring of the experimenter, robotic-arm manipulation, and real-time feedback of temperature and grip force.

We believe these supplementary videos provide a clearer and more intuitive demonstration of the integrated closed-loop system that encompasses multimodal sensing, mechanical control, and haptic reproduction.

Reviewer #3:

In this manuscript, Bai et al. report a polyvinyl alcohol hydrogel synthesized by a sequential solvent exchange process to achieve a highly soft, tough, and stretchable material. They demonstrate that their PVA hydrogel is responsive to a wide variety of stimulus, including temperature, mechanical, and ionic strength, which could make it an elegant single material solution for multimodal sensing. However, while the team presented the use of an active multimodal signal generator that employs machine learning to attempt to decouple confounding crosstalk between stimuli, rigorous characterization should also be conducted to understand how the sensor is influenced by various stimuli. Additionally, the supporting demonstrations for their human-machine interface should be extensively reported. The authors should address the following comments before further consideration.

Response: We sincerely appreciate the reviewer's careful evaluation of our manuscript. In response to your valuable suggestions regarding the influence of different stimuli on sensor performance and the demonstrations of the human–machine interface, we have provided point-by-point clarifications and added the necessary supplementary results, as detailed below.

Comment 3.1: The authors note that "the PVA hydrogel is engineered into a novel prismatic architecture." This structure does not appear to be novel as in the recent report (Nat Commun 2023, 14, 2907), and other similar pyramidal structures are commonly employed in pressure sensors.

Response: We sincerely appreciate the reviewer's thoughtful comment. Prismatic architecture have indeed been explored in serval papers on sensor design. As you have pointed out, in the work by Yang *et al.*, gradient pyramid electrodes were developed to broaden the linear sensing range and enhance the sensitivity through a capacitive mechanism [Nat. Commun. 14, 2907 (2023)]. However, we did not intend to claim novelty for the prismatic structure itself; instead, our contribution lies in employing this configuration to amplify vertical stress concentration and enable a d_{33}-mode piezoionic response.

Previous studies have shown the promise of piezoionic hydrogels for self-powered mechanoreception. Tuta *et al.* proposed the conversion of pressure into ionic current via the piezoionic effect to build a hydrogel-based artificial skin [Science 376, 502–507 (2022)]. Zhu et al. further demonstrated that stress concentration between rigid phases can promote charge separation, while the high ionic mobility in the soft and intermediate phases facilitates ionic transport [Adv. Mater. 36, 2313127 (2024)]. Although these studies highlight the potential of piezoionic hydrogels, the intrinsic

characteristic of the piezoionic effect is that when the hydrogel is deformed in-plane, pressure induces lateral ion migration, generating a charge imbalance primarily along the transverse direction, which corresponds to the d_{31} mode (Fig. R11a). Under vertical compression, the cubic hydrogel exhibits minimal stress concentration and weak directional convection, resulting in a limited d_{33} response (Fig. R11b). [Adv. Funct. Mater.33, 2300701 (2023)]. In contrast, our prismatic geometry concentrates stress at its apex, enhancing convection along the loading direction and thereby significantly improving the d_{33}-mode ionic output.

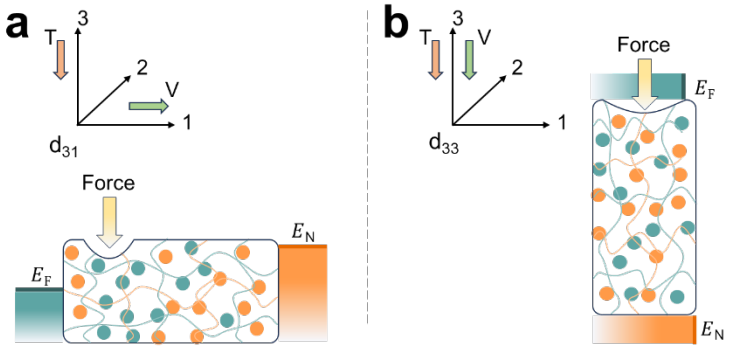

Fig. R11. The "d_{31} mode" (**a**) and "d_{33} mode" (**b**) of the piezoionic effect.

As a self-powered multimodal sensing device intended for skin attachment, both the thermogalvanic and diffusion effects naturally operate in the d_{33} mode (Fig. R12). In contrast, the piezoionic effect is limited by the weak d_{33} mode response under a cubic configuration.

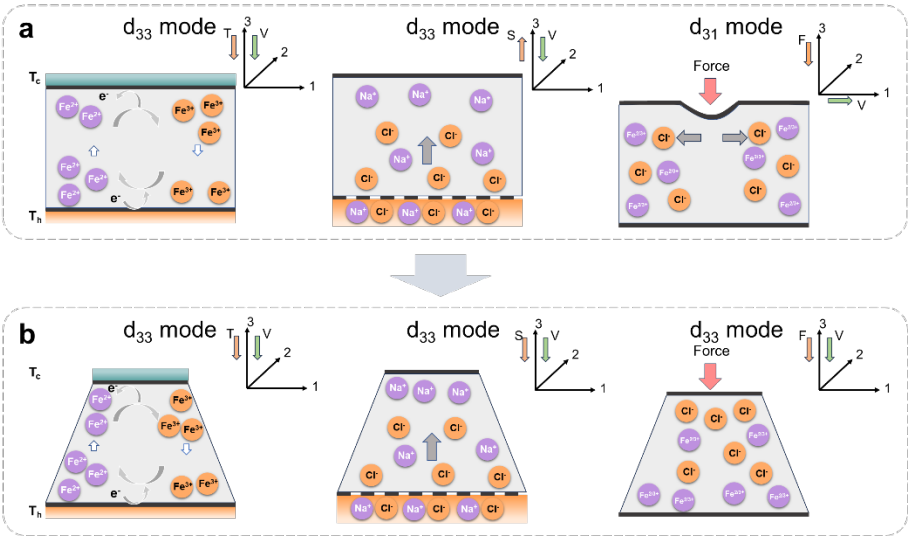

Fig. R12. Schematic illustrations of the thermogalvanic, diffusion, and piezoionic effects showing a transition from a mixed d31 and d33 configuration in (**a**) to a synergized d33 mode enabled by the prismatic architecture in (**b**).

To address this, we designed the prismatic architecture to significantly amplify the vertical stress concentration within the hydrogel (Fig. R13), thereby activating the d_{33} mode of the piezoionic effect and increasing the output current by over 100 times. This design enables the integrated acquisition of body temperature, pulse, and electrolyte signals within a single hydrogel system.

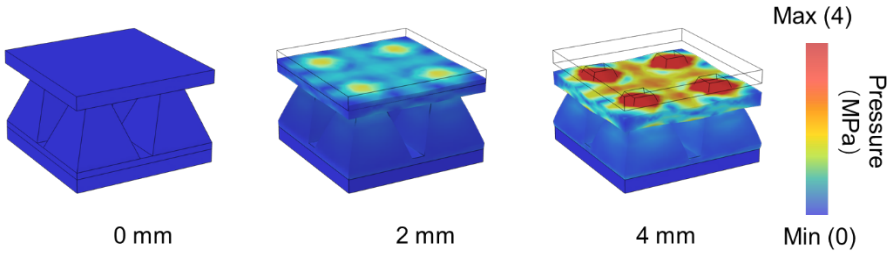

Fig. R13. COMSOL simulation of stress distributions in PVA hydrogels at increasing deformation.

We have added Fig. R11 to the Supplementary Information as Fig. S1.

Comment 3.2: The sequential solvent substitution process does not appear to have "clear advantages" over other methods, such as the solvent-exchanged-assisted wet annealing in their reference (Adv. Mater., 2023, 2210624). Similarly, this work introduced subsequential solvent exchange of PVA hydrogels from DMSO, glycerol, and an aqueous solution. Additionally, by tuning the solvent-exchange wet annealing process the work reported PVA hydrogels with similar properties: 100 kPa stiffness, MJ/m^3 toughness, 1000% strain.

Response: We sincerely thank the reviewer for the professional and important question.

We agree that "solvent-exchanged-assisted wet annealing" [Adv. Mater., 2023, 2210624] is an important and influential work, offering broad tunability of hydrogels to achieve high stiffness, high toughness, and large strain capability. As noted in their work, freeze–thaw hydrogels exhibit stiffness around 100 kPa but limited stretchability. In contrast, wet-annealed samples can achieve strains exceeding 1000%, though accompanied by increased rigidity and reduced water content. Therefore, our work aims for a targeted optimization, simultaneously considering properties including stiffness, water content, stretchability, and strength. Our objective is not to maximize mechanical strength alone. Instead, we aim to reduce rigidity while maintaining excellent tensile properties, yielding a mechanical profile more suitable for flexible electronic skin applications (Fig. R14).

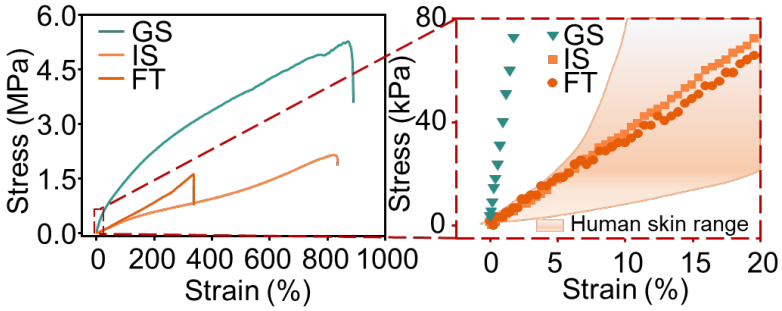

Fig. R14. Tensile stress–strain curves of PVA hydrogels after different solvent substitution treatments, compared to the range of human skin (orange shaded region).

More importantly, we aim to maintain high mechanical robustness while also achieving ionic conductivity and self-powered sensing, which imposes constraints distinct from methods focused purely on mechanical reinforcement. Efficient ionic transport and electrochemical activity require sufficient hydration and flexible polymer networks.

In wet-annealed hydrogels, increased crystallinity improves stiffness but can suppress or disrupt ionic pathways, thereby reducing conductivity and weakening signal sensitivity. Excessive crystallization also diminishes polymer-network mobility, making it difficult to support thermogalvanic, piezoionic, and diffusion-driven signal generation.

In contrast, our stepwise solvent-exchange strategy enables moderate crystallization for mechanical reinforcement while maintaining continuous hydrated ionic channels, achieving a balance between structural integrity and ion transport. For self-powered performance, the thermoelectric output relies on ionic diffusion and convective transport in the aqueous phase. Wet annealing unavoidably reduces the water content to ~55%–80%, which strongly impedes ion migration and suppressing thermoelectric output. Our dehydration experiments further verify that when the water content drops below ~80%, the Seebeck coefficient decreases significantly (Fig. R15), demonstrating that high hydration is essential for sustaining thermoelectric performance. Therefore, the solvent-exchange strategy adopted in this work helps retain high-water content to ensure a strong thermoelectric driving force.

In summary, the sequential solvent-exchange approach provides an effective balance among high hydration, ionic conductivity, and structural stability, enabling synergistic optimization of mechanical properties, transport performance, and energy-conversion efficiency to meet the demands of multifunctional integration.

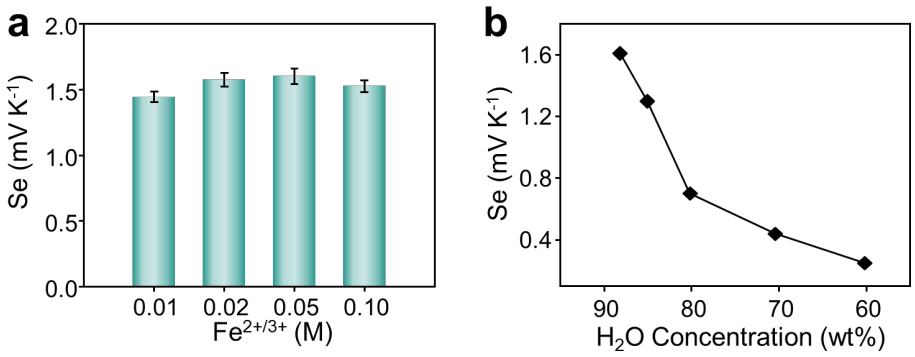

Fig. R15. **a** The Seebeck coefficient at increasing $Fe^{2+/3+}$ concentrations. **b** Seebeck coefficient varying with moisture content.

We have revised lines 266–268 on page 12 of the manuscript as follows: *"The high water content of the hydrogel also facilitated the thermogalvanic effect, as S_e would rapidly drop at lower water content (Fig. R15b)."* We have added Fig. R15 to the Supplementary Information as Fig. S11.

Comment 3.3: In figure 2j, the graph comparing properties of PVA hydrogels fabricated with other processes does not appear to be accurate, since solvent-exchanged-assisted wet annealing can similarly produce comparable soft hydrogels with <1MPa stiffness as mentioned.

Response: We sincerely thank the reviewer for the professional comment. In the original version, we inadvertently used the hydrogel sample annealed at 120 °C as a general representation of the wet-annealed condition, which led to an inaccurate comparison. We have now corrected this in the revised manuscript, and Fig. R16 has replaced the original Fig. 2j accordingly.

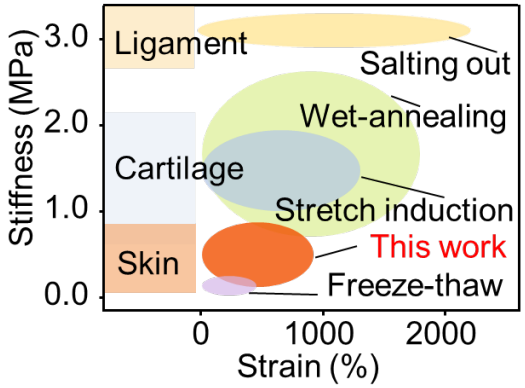

Fig. R16. Comparison of hydrogel toughness achieved in this study with that of various reported hydrogels and biological tissues.

Comment 3.4: For clarification, the authors note that "Electrolyte sensing was enabled by the diffusion effect, where temperature gradients led to differential ion diffusion." Did they mean that ionic gradients lead to ion diffusion?

Response: Thanks for pointing out this issue. We acknowledge that our previous wording was inaccurate. What we intended to convey is that the diffusion effect is primarily driven by the ion concentration gradient, which serves as the dominant force causing ions to migrate from regions of high concentration to low concentration. Furthermore, the temperature gradients induce the Soret effect, witch further enhances ion diffusion.

Specifically, when a temperature difference exists across the hydrogel, ions experience an additional thermodiffusion driving force, resulting in a larger ion flux than that produced by concentration-driven diffusion alone. To validate this, we compared diffusion currents under different temperature gradients and Na^+ concentrations (Fig. R17). The results show that when ΔT increased from 0 K to 2 K and 4 K, the measured diffusion current increased correspondingly under the same Na^+ concentration. This confirms that the concentration gradient is the dominant driver while the Soret effect further acts as an auxiliary enhancement.

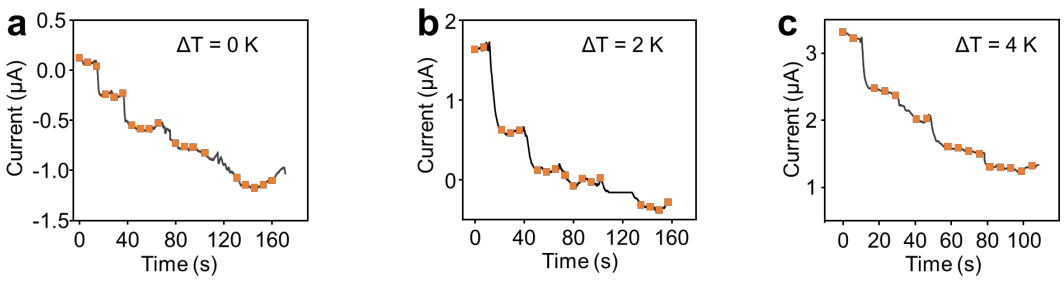

Fig. R17. Time-dependent diffusion current curves during stepwise absorption of 50μL Na^+ solutions at different temperature differentials: (**a**) 0 K, (**b**) 2 K, (**c**) 4 K. The cold junction temperature was fixed at 30 °C. The hot junction temperature was set to 30, 32, and 34 °C, respectively.

To avoid misunderstandings, we have revised lines 246–250 on page 11 of the manuscript as follows: *"Electrolyte sensing was enabled by the diffusion effect, where ion concentration gradients led to differential ion diffusion. As these mechanisms operated through distinct ion-driven processes, they could function independently in the same system with minimal interference, allowing for synergistic multimodal sensing."*

We also revised lines 385–387 on page 16 as follows: *"In addition, the ionic diffusion was further enhanced by the Soret effect, which arose from the temperature gradient between the skin and the ambient environment and led to differential ion mobility."*.

Comment 3.5: In figure S11, why is there still a current density when electrode distance = 0mm? Aren't the electrodes shorted?

Response: Thank you for pointing out these issues. We realize that the annotation in our original manuscript may have been misleading. The Δd on the horizontal axis in Fig. R18 actually represents the distance between the sensing electrode and the heat source, which was used to evaluate the non-contact temperature-sensing capability. Therefore, $\Delta d = 0$ mm indicates direct contact between the heat source and sensing unit, rather than a zero distance between the two electrodes. Meanwhile, the hot and cold electrodes remain fixed at opposite ends of the PVA hydrogel and do not touch each other, ensuring no short circuit occurs.

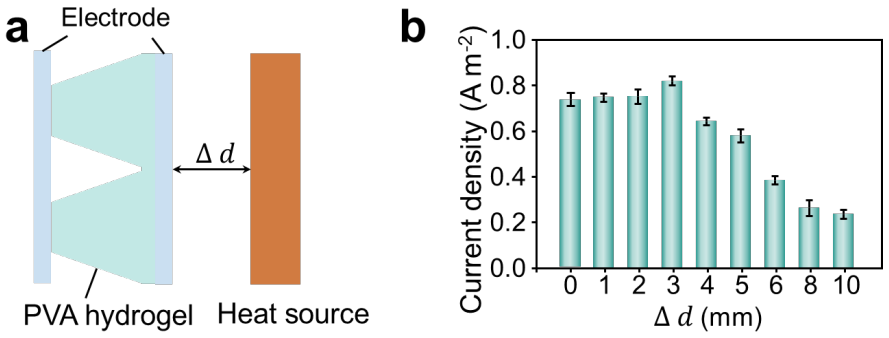

Fig. R18. Non-contact Temperature Sensing Test. a Current density changes as the distance between the hydrogel e-skin and the heat source decreases from 10 mm to full contact (0 mm). d is the distance from the heat source to the hot end electrode of the gel. **b.** The current magnitude depends on the temperature difference between the hot and cold ends. At smaller distances, heat radiation raises the cold-end temperature, reducing the temperature difference and lowering the output current.

We have clarified the definitions of Δd in the supporting materials and added Fig. R18 as Fig. S13. The description on page 12, lines 293–296 has been revised to: *"Since the distance from the heat source could also affect output, the highest current density was found at a 3-mm distance, with lower performance observed at both closer and further distances due to a reduced temperature gradient (Fig. R18)."*

Comment 3.6: Could the authors clarify this calculation: "the maximum output power density (Pmax) was calculated as 19 $\mu W \cdot m^{-2} \cdot K^{-2}$," since this value and units differ from the power density in figure 3d.

Response: Thank you for pointing out this issue. The discrepancy in units arose because the original manuscript did not clearly distinguish between the calculation method for power density and normalized power density, which may cause confusion for readers. Both calculations are used to evaluate power density, with the former providing the actual power per unit area and the latter offering a normalized value that removes temperature dependence for comparative purposes. In the revised manuscript, we have clearly distinguished the two quantities and added the theoretical formulas for calculating the maximum output power density ($P_{\max}$) and the normalized power density ($P_{\max}\,\Delta T^{-2}$) (Fig. R19). The revision is as follows:

*"**Theoretical calculation of the maximum output power density (P_{max}) and the normalized power density ($P_{max}\,\Delta T^{-2}$):***

For the theoretical calculation of P_{max}:

$$P_{max} = \frac{V_{oc} \times I}{4} \qquad R(1)$$

in which

$$I = \frac{I_{SC}}{A} \qquad R(2)$$

where V_{oc} is the open-circuit voltage, I is the current density, I_{SC} is the short-circuit current, and A is the cross-sectional area.

With P_{max}, the normalized power density ($P_{max}\,\Delta T^{-2}$) can be calculated as

$$\frac{P_{max}}{\Delta T^2} = \frac{V_{oc} \times I}{4 \times \Delta T^2} \qquad R(3)$$

where ΔT is the temperature difference between hot and cold ends."

R(1), R(2), R(3) are replaced with (3), (4), (5) in the supporting information respectively.

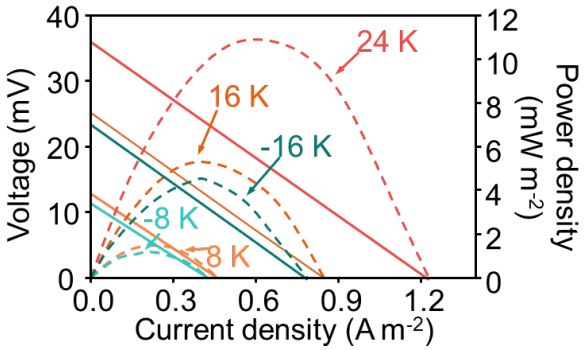

Fig. R19. Output voltage-current curves and corresponding power densities under various temperature gradients.

The revised text is detailed on page 12, lines 290–292: *"Based on these measurements, the maximum output power density (P_{max}) was calculated as 11 mW·m^{-2}, with the normalized power density ($P_{max}\ \Delta T^{-2}$) reaching 19 μW·m^{-2}·K^{-2}."*

Comment 3.7: In figure 3g, how does the prismatic structure result in 100x sensitivity? Is this for the same load or the same strain?

Response: Thank you for raising this question. The 100-fold increase in output current shown in Fig. 3g was obtained under identical load conditions, and the enhancement arises directly from the prismatic structural design.

Specifically, the piezoionic effect originates from ion redistribution during deformation. In our hydrogel system, the relatively large anions experience stronger steric hindrance from the polymer network, resulting in localized ionic accumulation during mechanical deformation. Due to stress-induced asymmetric ionic mobility, anions and cations migrate at different rates, forming a transient ionic concentration gradient and an internal electric field.

To exploit this effect, we introduced a prismatic architecture to amplify vertical stress concentration. Under compression, the anisotropic geometry promotes a larger mobility difference between cations and anions along the loading direction, establishing a stronger ionic gradient and a higher piezoionic current. We compared cubic and prismatic hydrogels with identical cross-sectional areas under the same applied load (30 N) (Fig. R20). The prismatic hydrogel produced a peak piezoionic current exceeding 80 μA, whereas the cubic hydrogel generated less than 1 μA, demonstrating the significant amplification enabled by the prismatic design.

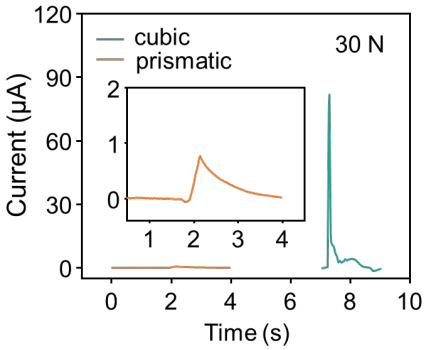

Fig. R20. For hydrogel structures with cubic and prismatic shapes having identical cross-sectional areas, the time-dependent relationship of the piezoionic current under identical load of 30N.

We have revised lines 317-321 on page 13 of the manuscript as follows: *"Further leveraging this, the prismatic structure design was introduced to amplify the vertical stress concentration, generating an electric field along the force direction (d33 mode). Compared to the cubic structure, this design achieved over a hundredfold increase in output current under identical stress conditions (Fig. 3g and Fig. R20).".* Fig. R20 has been added to Fig. S20 in the Supplementary Information.

Comment 3.8: How does the prismatic structure affect the performance of thermogalvanic and electrolyte sensing compared to cubed structure?

Response: Thank you for the thorough review and valuable comments. To more comprehensively evaluate the effects of geometric design, we compared the thermogalvanic and electrolyte-sensing performance of cubic and prismatic hydrogel units with the same base areas and heights. The results are summarized below:

Thermogalvanic sensing:

The prismatic structure has a smaller effective contact area at the top surface, which reduces the active electrode–electrolyte interface. Since thermoelectric conversion relies on Fe^{3+}/Fe^{2+} redox kinetics at this interface, the reduced contact area lowers the electron-exchange rate and increases the equivalent impedance, leading to a slightly lower output current compared to the cubic structure. Nevertheless, both geometries exhibited stable and nearly linear thermoelectric response (Fig. R21), indicating that the prismatic geometry affects only the output amplitude of the thermoelectric current without altering the intrinsic thermodynamic mechanism.

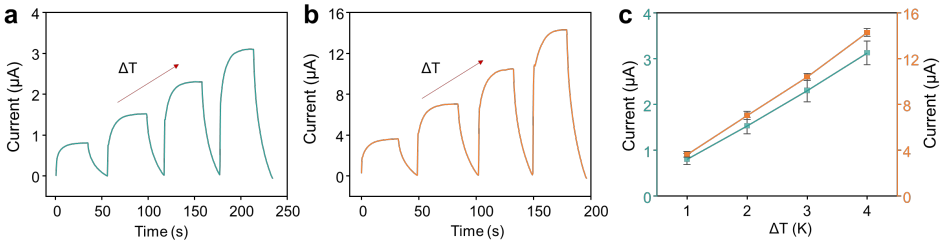

Fig. R21. Thermoelectric current comparison between prismatic (**a**) and cubic (**b**) structures. **c** Thermoelectric current against temperature difference in prismatic and cubic structures. The cold-end temperature is fixed at 30 °C.

Electrolyte sensing:

Electrolyte sensing is primarily driven by Na^+ concentration-gradient-induced diffusion, governed by chemical potential gradients and bulk ionic transport pathways. Unlike thermoelectric conversion, Na^+ transport occurs mainly within the hydrogel matrix rather than at the electrode interface. Therefore, the macroscopic geometric differences

do not significantly affect the ionic transport pathways and solvation environments [Chem. Sci. **12**, 12874-12910 (2021)]. As a result, both geometries produce nearly identical diffusion currents under passive sensing conditions, demonstrating that diffusion-based electrolyte sensing is largely insensitive to geometric topology (Fig. R22).

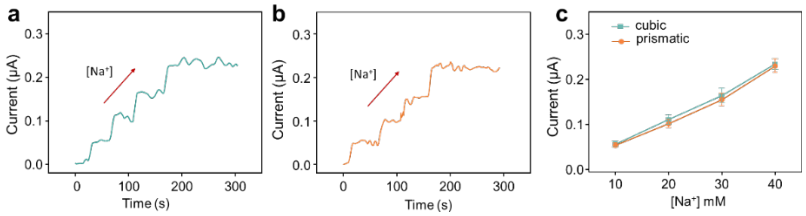

Fig. R22. Diffusion current comparison Between Prismatic (**a**) and Cubic (**b**) Structures. **c** Diffusion current against Na^+ concentration in prismatic and cubic structures. Hydrogel temperature maintained at 30 °C.

In addition, Fig. R21 has been added in the Supplementary Information as Supplementary Fig. S19. Page 13, lines 306–309 of the manuscript are supplemented as follows: *"Although the final prismatic structure could slightly reduce thermoelectric currents compared with simple cubic blocks—due to the smaller electrode contact area at the apexes and higher overall resistance from the reduced volume—it still maintained a robust linear response (Fig. R21)."*

Fig. R22 has been added in the Supplementary Information as Fig. S34. Page 16, lines 394–396 of the manuscript are supplemented as follows: *"Compared with cubic shapes, the prismatic structure showed no significant difference in ion diffusion currents, as its ion transport distance remained similar to that in solvated environments (Fig. R22)."*

Comment 3.9: Critically, for simultaneous multimodal sensing, characterizations should be conducted while manipulating one stimulus at a time to observe their influence on the current output measurements. For instance, ionic concentration of NaCl can also influence the sensitivity of thermogalvanic and piezoionic effects.

In figure 3d, how is this signal decoupled into the temperature, pressure and Na concentrations? It seems that the compound current raw recordings should simply be a superposition from all the inputs from thermogalvanic, piezoionic, and electrolyte stimuli. The compound signal does not appear to encode any of the high frequency responses in the plot of the current corresponding to pressure below. Likewise, the lower frequency current contributions from the temperature sensing component does not in the compound recording.

It seems unclear how different stimuli together are influencing the output. Rather than solely relying on a machine learning to "decouple" these, rigorous characterization should be further investigated.

Response: Thanks for your insightful comment on the durability of our multimodal sensors. We agree that using controlled-variable experiments to examine how individual stimuli affect the current output is crucial for deconstructing how these signals collectively influence the overall response mechanism. Therefore, we first performed a series of controlled experiments to quantify the effect of each stimulus on the output current and to identify any potential interference among the different sensing modalities.

According to liquid thermoelectric theory, the Seebeck coefficient $S_e = \Delta E/\Delta T = \Delta S_{rc}/nF$, where $\Delta S_{rc}$is the entropy change of the redox couple, $n$is the electron-transfer number, and $F$is the Faraday constant [J. Mater. Chem. A 10, 19690–19698 (2022)]. Within the moderate temperature range used in this study, the thermovoltage increases proportionally with the temperature difference. In contrast, the pressure-driven piezoionic response originates from transient directional ion migration caused by local network deformation. Smaller cations move more rapidly through the polymer matrix than larger anions, resulting in charge imbalance, local concentration and potential gradients, and a chemical potential gradient that scales with the applied stress. The diffusion-induced signal follows Fick's law and varies linearly with the Na^+ concentration gradient, while the microchannel design ensures stable transport without reaching adsorption saturation. These three mechanisms therefore operate independently at distinct spatial and temporal scales, producing characteristic current profiles that provide the basis for subsequent signal decoupling.

Manipulating pressure signals under varying temperature differences:
The piezoionic current was measured under various temperature differences while fixing the cold end at 30 °C (Fig. R23a, b). Without a temperature gradient, pressures of 2–8 kPa generated currents of 0.8–2.7 μA. As ΔT increased, a baseline thermoelectric current appeared; however, the pressure-induced increments ΔI remained nearly unchanged. This independence arises from different transport pathways: thermogalvanic signals emerge from temperature-driven redox reactions occurring over seconds, whereas piezoionic currents result from rapid, localized ionic polarization within milliseconds.

Manipulating pressure signals under varying electrolyte concentrations:
Similarly, increasing Na^+ concentration increased the diffusion-driven current, but the pressure-induced ΔIremained almost identical at all tested concentrations (Fig. R23c, d). Diffusion is a slow, steady-state process governed by concentration gradients, whereas the piezoionic effect derives from transient stress-induced polarization. Because they occur on distinct timescales and through different transport pathways, the pressure response is not affected by Na^+ concentration.

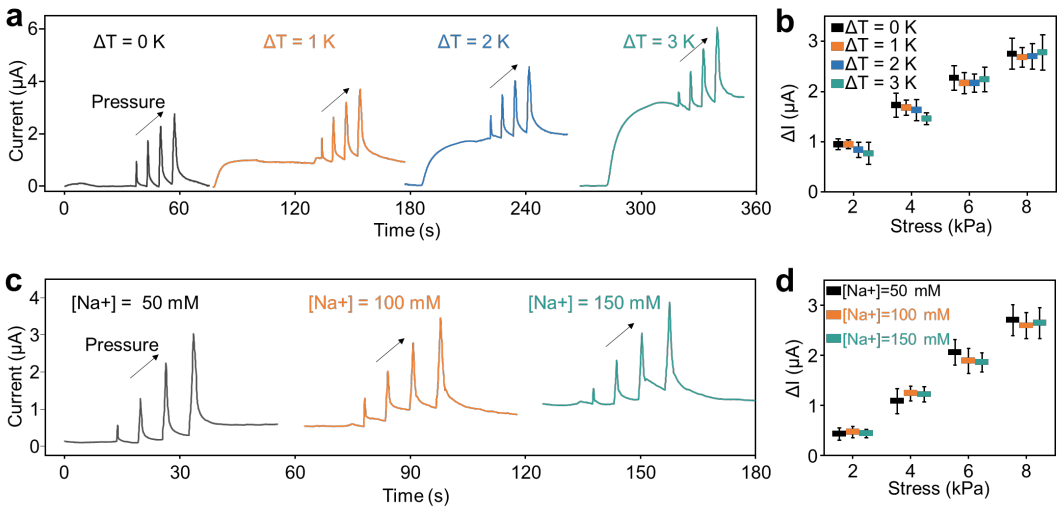

Fig. R23. a Piezoionic current at different temperature levels, where the cold end temperature is set to 30 °C, while the hot end temperatures are set to 30, 31, 32, and 33 °C, respectively. The applied pressures are 2, 4, 6, and 8 kPa, respectively. **b** Relationship between pressure and current variation (ΔI) at different temperature levels (ΔT). **c** Piezoionic current under different Na^+ concentrations, with applied pressures of 2, 4, 6, and 8 kPa, respectively. **d** Relationship between pressure and current variation (ΔI) under different Na^+ concentrations.

Manipulating temperature differences signals under varying electrolyte concentrations:

Increasing Na^+ concentration enhanced the thermogalvanic current, while larger temperature differences increased the diffusion-driven current (Fig. R24). This coupling stems from the synergistic action of the Soret effect and the thermogalvanic effect [Science 368, 1091–1098 (2020)], which can be described by $J = -D\nabla c - D_T c\nabla T$. Temperature gradients drive Na^+ ions toward the colder end, adding a thermodiffusion component to the overall flux. At the same time, elevated temperature accelerates concentration-driven diffusion. Within the tested temperature range, both contributions remain linear and superimpose additively. For example, at Na^+ concentrations of 50, 100, and 150 mM, the thermoelectric currents under a 1 K temperature difference were 0.89, 1.05, and 1.39 μA; under 2 K they increased to 1.82, 2.10, and 2.70 μA. These results suggest an additional ~0.15 $\mu A \cdot K^{-1}$ per 50 mM Na^+, consistent with the measured 4.5 μA thermoelectric current at 100 mM and 4 K.

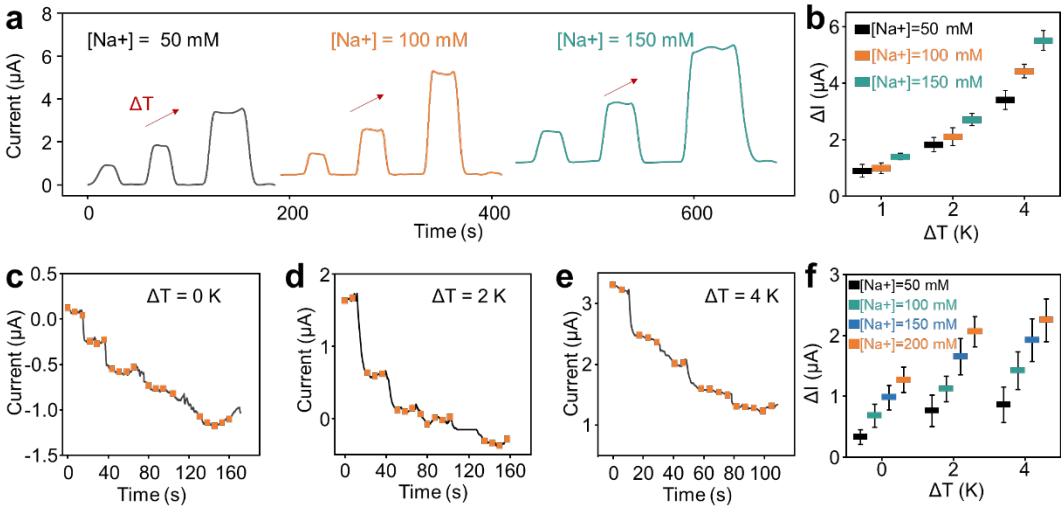

Fig. R24. a Thermoelectric current induced by different temperature differences at various Na^+ concentrations, with the hot junction temperature fixed at 30 °C. The cold junction temperatures were set to 29, 28, and 26 °C, respectively. **b** Thermoelectric response under different Na^+ concentrations. Time-dependent diffusion current curves during stepwise absorption of 50μL Na^+ solutions at different temperature differentials: (**c**) 0 K, (**d**) 2 K, (**e**) 4 K. The cold junction temperature was fixed at 30 °C. The hot junction temperature was set to 30, 32, and 34 °C, respectively. **f** Effect of Na^+ concentration on diffusion current variation (ΔI) under different temperature differences (ΔT).

This discussion has been added to page 19 of the manuscript, lines 442–456, as follows: *"To investigate potential crosstalk between the signals, we applied repeated pressure stimuli of 2, 4, 6, and 8 kPa under different temperature gradients (Fig. S35a) and different Na+ concentrations (Fig. S35b). The piezoionic current increments remained nearly identical in all cases, indicating that the pressure-induced ionic signals were not affected by variations in temperature nor Na^+ concentration. This independence arose from the distinct physical origins of the signals: the piezoionic current was generated by transient, mechanically induced ionic polarization, whereas the thermoelectric and diffusion currents were driven by inherently slow, steady-state processes. A minor interaction was observed between the temperature and Na^+ concentration signals: a larger temperature gradient produced higher diffusion currents because temperature not only drove the thermogalvanic potential but also triggered the Soret effect, causing additional Na+ migration along the thermal gradient (Fig. S36). Nevertheless, within the temperature range investigated in this work, both temperature- and concentration-driven diffusion remained in the linear regime, which allowed their contributions to superimpose proportionally and produce a stable, predictable current response."*

Fig. R23 have been added in the Supplementary Information as Fig. S35. Fig. R24 have been added in the Supplementary Information as Fig. S36.

Regarding the reviewer's question about Fig. 3d, we agree that the composite signal represents a superposition of thermoelectric, piezoionic, and electrolyte-stimulated signals. Because the three stimuli operate through independent transport pathways and exhibit distinct temporal signatures—sharp spikes for pressure, step-like plateaus for temperature, and slow drifts for Na^+ diffusion—the composite waveform retains identifiable features from each stimulus. Also as confirmed by our control experiments, the piezoionic response shows negligible interference with both diffusion and thermoelectric currents. Likewise, the diffusion and thermoelectric currents exhibit distinct different magnitudes, and the influence of Na^+ concentration under various temperature gradients remains linearly correlated with the temperature difference. Together, these characteristics minimize mutual interference and allow the coupled current waveform to be interpreted as a superimposed signal containing three independent modal contributions.

To further demonstrate the signal decoupling capability of our system, we conducted additional experiments using smaller stimulus intensities, applying pressures of 0–3 N, temperature differences of 0–4 °C, and Na^+ concentrations of 0–100 mM (Fig. R25). Stimuli were applied sequentially in the order of Na^+, temperature, and pressure. The resulting composite current exhibited distinct features corresponding to each stimulus: sharp transient spikes under pressure, stepwise variations under temperature, and gradual components induced by Na^+ diffusion.

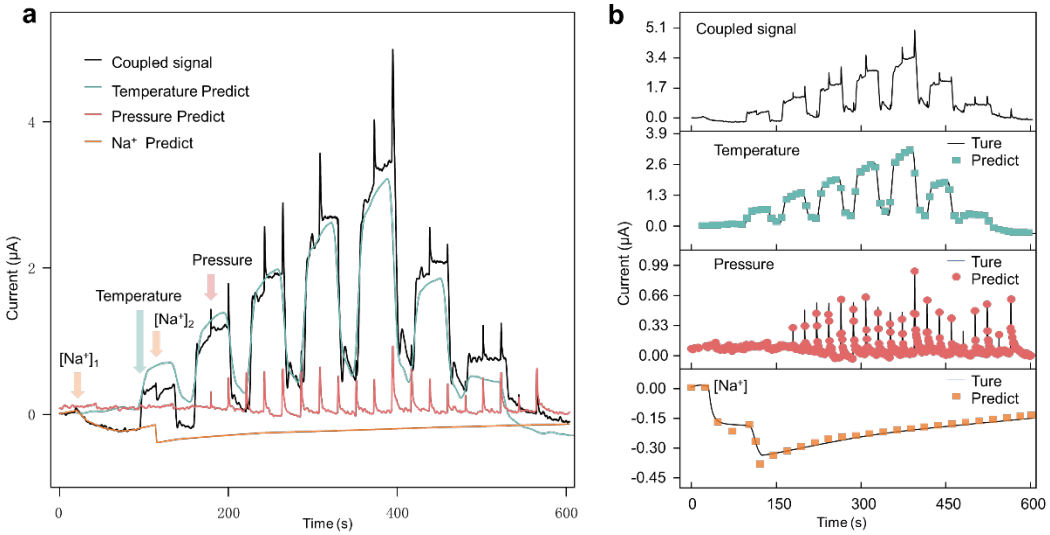

Fig. R25. a Coaxial plots of coupled signals and prediction curves for small variations in electrolyte, temperature, and pressure. Temperature was fixed at 30°C at the cold end, while the hot end varied from 30°C to 35°C. Pressure ranged from 0 to 3 N, and Na^+ concentration varied from 0 to 100 mM in two permeation steps. **b** Comparison of coupled signals and LSTM prediction results for electrolyte, temperature, and pressure on the same X-axis.

To quantitatively decouple these signals, we employed a multilayer long short-term memory (LSTM) neural network integrated with a local attention mechanism. The continuous current signal was segmented into fixed-length windows of 40 s as model inputs. At each time step *t*, the local attention module computed similarity scores *e(t, j)* between the current signal and its neighboring time frames within the range [t − 40, t + 40], and then converted them into attention weights *α(t, j)* through a softmax function. This mechanism adaptively focuses on the most relevant local segments while effectively suppressing long-range noise, thereby enhancing the extraction of modality-specific features.

$$e_{t,j} = score(s_t, s_j), j \in [t-40, t+40] \quad R(4)$$

$$c_t = \sum_j \frac{\exp(e_{t,j})}{\sum_k \exp(e_{t,k})} S_j \quad R(5)$$

$$x_t = [s_t, c_t] \quad R(6)$$

Subsequently, a three-layer stacked LSTM network was used, where each unit contains a forget gate (f_t), input gate (i_t), output gate (o_t), and cell state (C_t). The forget gate controls how much of the historical state is retained, the input gate regulates the incorporation of new information, and the output gate determines the effective output at each time step. Through this gated mechanism, the LSTM can capture both short-term transient responses (e.g., pressure-induced ionic polarization) and long-term steady changes (e.g., temperature or Na^+ diffusion). The multimodal features are encoded into the cell state vector C_t, representing the evolving state of multiple stimuli over time.

$$f_t = \sigma[W_f \cdot [h_{t-1}, x_t] + b_f] \quad R(7)$$

$$i_t = \sigma[W_i \cdot [h_{t-1}, x_t] + b_i] \quad R(8)$$

$$\widetilde{C_t} = \tanh[W_C \cdot [h_{t-1}, x_t] + b_C] \quad R(9)$$

$$C_t = f_t * C_{t-1} + i_t * \widetilde{C_t} \quad R(10)$$

After feature extraction, a three-layer fully connected network (FCN) was appended to the model. The FCN performs nonlinear mapping from each LSTM hidden state to three independent outputs corresponding to temperature, pressure, and Na^+ electrolyte concentration. As a result, the model can achieve real-time separation and quantitative reconstruction of the mixed current signal at each moment, effectively decomposing it into three independent physical components. This enables the independent recognition and dynamic tracking of multimodal stimuli in real time.

Fig. R25 have been added in the Supplementary Information as Fig. S37. This discussion has been added to page 21 of the manuscript, lines 496–499, as follows:

"When temperature, pressure, and Na^+ electrolyte stimuli in their characteristic patterns were simultaneously applied to the AMSG, the resulting compound current signal was accurately decoupled into distinct components corresponding to each stimulus (Fig. 4d and Fig. S37)."

Comment 3.10: In figure 5g, does the sensor contact the heat and cold source? Why is there no apparent change in the current recording in response to pressure?

Response: Thank you very much for your questions. In Fig. 5g, the sensor does not contact either the heat or cold source, which is why no pressure-induced current variation is observed in the recording.

This experiment was specifically designed to evaluate non-contact temperature sensing; thus, only thermal radiation from the object induces a temperature gradient across the hydrogel, generating a thermoelectric current (Fig. R26). By analyzing the real-time current feedback during approach, the system can distinguish between safe and hazardous temperature zones. When the detected temperature exceeds a preset threshold, the wristband provides thermal warning and vibrotactile feedback alerts the users to prevent grasping overheated objects.

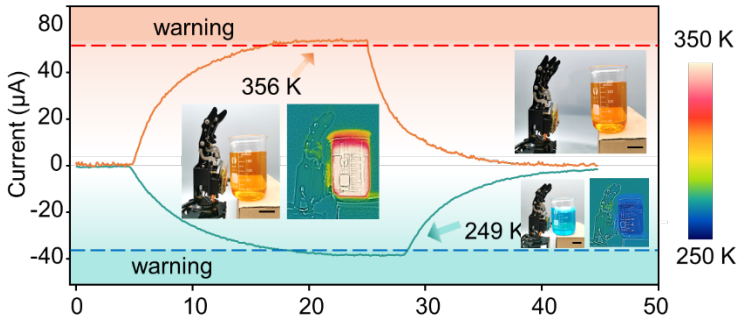

Fig. R26. Current signals of the AMSG as the robotic hand approaches or retreats from heat or cold sources, illustrated by optical and infrared images.

The feedback signal for the grasping process involving contact with hot source is shown in Fig. R27 (Fig. 5h in the manuscript). It further demonstrates a representative application scenario of the AMSG wristband that integrates sensing, haptic feedback, and safety-protection functions. The entire workflow produces a characteristic three-stage current profile: (1) non-contact temperature prediction, (2) contact-based accurate temperature sensing, and (3) grip-force sensing.

As the robotic hand approached a paper cup filled with hot water, the current signal gradually increased to ~14 μA. If the detected temperature remained within a safe range, grasping proceed; otherwise, robotic motion was stopped. Upon contact, the current

rose to ~30 μA due to the sudden temperature increase. Meanwhile, the thermal actuator on the user side was triggered to reproduce the detected temperature. A similar response could also be achieved for cold objects, enabled by the polarity of the thermoelectric signal.

In addition, the safety mechanism also extends to pressure sensing. During grasping, a current exceeding ~45 μA indicates excessive gripping force. By monitoring this threshold, the system can avoid over-compression of fragile objects. The complete grasping process is shown in Supplementary Video 3-5.

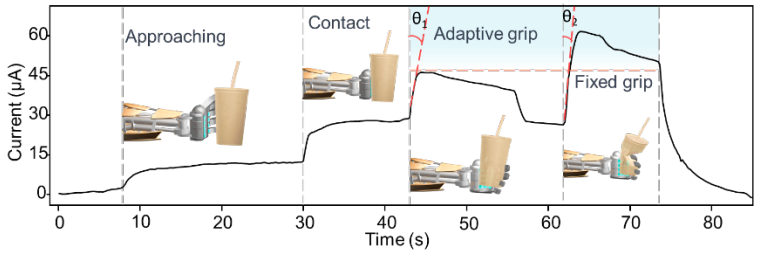

Fig. R27. Current signals of the AMSG as the robotic hand approaches or retreats from heat or cold sources, illustrated by optical and infrared images.

To improve clarity, we have revised the description on lines 579–589 of page 24 in the manuscript to *"The entire workflow produced a three-stage current profile: (1) non-contact temperature sensing, (2) contact-based accurate temperature sensing, and (3) grip-force sensing (Video S5). As the robotic hand approached a paper cup filled with hot water, the current signal gradually increased to 14 μA. If the detected temperature remained within a safe range, the grasping action would proceed; otherwise, robotic motion would be stopped. Upon contact, the current rose to 30 μA due to the sudden temperature increase. Meanwhile, the thermal actuator at the user end was triggered to reproduce the detected temperature. A similar response could also be achieved for cold objects, enabled by the polarity of the thermoelectric signal. In addition, the safety feature was integrated in the pressure sensing feedback. For specific objects, an adaptive grasping action generated a piezoelectric signal below a set threshold."*

Comment 3.11: Are there any supporting videos for figure 5f for real-time linear motor control from sensor feedback? Are there additional videos to accompany figure 5h to show responsive robotic hand control according to feedback? Further supporting videos should better demonstrate "closed-loop" functionality.

Response: Thank you for your valuable feedback and suggestions. Following your advice, we have added more videos in the supplementary materials to more

comprehensively demonstrate the real-time control and closed-loop functionality of our system.

Supplementary Video 3 presents the complete demonstration associated with Supplementary Fig. 5h. The workflow exhibits three distinct signal stages: (1) non-contact temperature prediction, (2) contact-based accurate temperature sensing, and (3) grip-force sensing. As the robotic hand approaches a cup containing hot water, the thermoelectric current increases progressively, enabling real-time temperature prediction and immediate decision-making on whether the grasping action should proceed. If the temperature exceeds the safe threshold, the system terminates the motion instantly. Upon contact, the current rises sharply, allowing real-time identification of the actual object temperature. During gripping, the piezoionic response produces a larger and faster current change, which the system uses in real time to regulate gripping force and prevent excessive compression.

Supplementary Video 4 corresponds to Fig. 5f shows the linear vibration-control behavior. Under different gripping forces, the vibration module presents clearly distinguishable different vibration amplitudes and frequencies in a real time.

Supplementary Video 5 demonstrates a complete closed-loop human-machine interaction scenario. It showcases remote handling of hazardous chemicals, integrating physiological monitoring of the operator, robotic-arm manipulation, and real-time reproduction of temperature and grip-force feedback.

All videos are uploaded in the supplementary materials. We believe that these additional videos provide a clearer and more intuitive demonstration of the real-time control and closed-loop capabilities of the AMSG system.